

Article

Synthesis of rGO/CoFe₂O₄ Composite and Its Magnetorheological Characteristics

Yang Lv ¹, Chengjie Gong ¹, Yuzhen Dong ^{1,*} and Hyoung Jin Choi ^{2,*}

¹ School of Materials Science and Engineering, Harbin Institute of Technology Weihai, 2 West Wenhua Road, Weihai 264209, China; 2021211612@stu.hit.edu.cn (Y.L.); 2021211658@stu.hit.edu.cn (C.G.)

² Department of Polymer Science and Engineering, Inha University, Inha 22212, Republic of Korea

* Correspondence: yuzhend@hit.edu.cn (Y.D.); hjchoi@inha.ac.kr (H.J.C.)

Abstract: In this study, composite particles of rGO/CoFe₂O₄ were synthesized using a solvothermal method to fabricate a low-density magnetorheological (MR) material with enhanced sedimentation stability. The morphology and crystallographic features of rGO/CoFe₂O₄ were characterized via SEM, TEM, and XRD, and its magnetic properties were tested using VSM. The MR fluid was formulated by blending rGO/CoFe₂O₄ particles into silicone oil. Under different magnet strengths (H), a rotational rheometer was used to test its MR properties. Typical MR properties were observed, including shear stress, viscosity, storage/loss modulus, and dynamic yield stress (τ_{dy}) following the Herschel–Bulkley model reaching 200 Pa when H is 342 kA/m. Furthermore, the yield stress of the MR fluid follows a power law relation as H increases and the index changes from 2.0 (in the low H region) to 1.5 (in the high H region). Finally, its MR efficiency was calculated to be about 10⁴% at H of 342 kA/m.

Keywords: rGO; CoFe₂O₄; composite; magnetorheological; yield stress

1. Introduction

Magnetorheological (MR) fluids are usually suspensions of magnetic particles distributed in a base liquid [1]. As a class of magnetically responsive smart materials, MR fluids are widely valued for their unique MR effect [2,3]. Upon applying or removing an external magnetic field (H), MR fluids can convert between a liquid and a solid-like state within milliseconds [4]. When H is applied, the magnetic particles within MR fluids are polarized. The magnetic dipoles interact and organize into chain-like structures along the H direction. These chain-like structures resist flow and increase viscosity, making MR fluids a solid-like state [5]. When H is removed, MR fluids return to a liquid state. The characteristics of MR fluids find application across various engineering domains, such as dampers or shock absorbers [2], polishing [6], vehicle suspension [7,8], biomedical applications [9], soft robots [10], MR electrolytes in batteries [11], and so on. Moreover, the millisecond response time of MR fluids makes them one of the most rapid electromechanical interfaces [12]. Carbonyl iron (CI) particles are extensively utilized when preparing MR fluids due to their high saturation magnetization, ease of synthesis, and other favorable properties [13]. Nevertheless, MR fluids utilizing CI particles face a notable problem of magnetic particle sedimentation, which causes a considerable reduction in the MR effect [12–14]. Cobalt ferrite (CoFe₂O₄) is a cubic spinel-structured ferrite widely studied for its excellent electromagnetic properties and application characteristics in electronic products [15]. Meanwhile, CoFe₂O₄, with low density and excellent magnetic characteristics, has also attracted widespread attention for its MR performance [16,17].

Graphene, a two-dimensional (2D) material, has been extensively researched for its excellent electronic transport properties [18–20], mechanical properties [21,22], thermal conductivity [23], optical transparency [24], and other properties [25]. These properties enable graphene to have broad application prospects in important fields, including medicine,



Citation: Lv, Y.; Gong, C.; Dong, Y.; Choi, H.J. Synthesis of rGO/CoFe₂O₄ Composite and Its Magnetorheological Characteristics. *Materials* **2024**, *17*, 1859. <https://doi.org/10.3390/ma17081859>

Received: 15 March 2024

Revised: 9 April 2024

Accepted: 13 April 2024

Published: 18 April 2024



Copyright: © 2024 by the authors. Licensee MDPI, Basel, Switzerland. This article is an open access article distributed under the terms and conditions of the Creative Commons Attribution (CC BY) license (<https://creativecommons.org/licenses/by/4.0/>).

sustainable energy, composite materials, and so on [26–28]. A highly utilized graphene production approach is employing graphene oxide (GO) as a precursor, followed by removing oxygen-based functional groups from the GO surface through thermal or chemical reduction methods [29,30]. GO can be obtained by oxidation of natural graphite. This process introduces reactive oxygen-based functional groups, including hydroxy, carboxyl, epoxide, and carbonyl groups, onto the basal planes and borders of the graphene-derived layers, increasing the distance between layers [31,32]. In particular, it has been widely noted that these reactive functional groups are helpful when synthesizing GO-based composite materials, such as the synthesis of RGO-Fe₃O₄ composite [33], graphene oxide/polyethylene glycol composite [34], Cellulose–Graphite Oxide Composite [35], and so on.

A nanocomposite consisting of CoFe₂O₄ nanoparticles and rGO, characterized by outstanding magnetic properties, a large specific surface area, and low density, can enhance the MR fluid's sedimentation stability and is expected to demonstrate typical MR behavior. This study utilized a modified Hummer's method [36] to synthesize GO. In order to avoid the difficulty of dispersion in silicone oil caused by oxygen-based functional groups in GO, GO was reduced to reduced graphene oxide (rGO) [37]. Finally, the rGO/CoFe₂O₄ composite synthesized via a solvothermal method was dispersed into silicone oil to study its MR characteristics under different H .

2. Materials and Methods

2.1. Synthesis of Graphene Oxide (GO)

The synthesis of GO followed a modified Hummer's method [36]. A quantity of 2 g of sodium nitrate (NaNO₃) and graphite (4 g) were dispersed in 280 mL sulfuric acid (H₂SO₄) to obtain a homogeneous suspension with intense stirring. Then 12 g of potassium permanganate (KMnO₄) was introduced into the suspension, followed by 30 min of stirring and 15 min of sonication. The obtained mixture was slowly poured into 700 g of water in a fume hood, and then a hydrogen peroxide (H₂O₂) solution (200 g of H₂O₂ dissolved in 400 water) was introduced. The reaction solution was slowly stirred for 20 min, and centrifugation was used to wash the product with water until the pH was constant. Finally, the resulting GO block was dispersed in water, peeled off into GO sheets via sonication for 4 h, and freeze-dried.

2.2. Fabrication of Reduced GO/Cobalt Ferrite (rGO/CoFe₂O₄)

GO (0.5 g) was dispersed in H₂O (150 mL) following 1.5 h of sonication while stirring. Next, Fe(NO₃)₃ (6.875 g) and Co(NO₃)₂ (2.475 g) were introduced, and the mixture's pH was adjusted to 10. The reaction solution was moved to an autoclave and subjected to heating at 180 °C. After an 18 h reaction, it was cooled to room temperature. Then a water wash was performed with magnetic separation. Finally, the drying process was carried out.

2.3. Preparation of MR Fluid

The MR fluid was formulated by blending 10% volume of rGO/CoFe₂O₄ particles into 1000 cSt silicone oil. The MR fluid was then subjected to shaking (VORTEX Genius 3, IKA, Staufen, Germany) and sonication (Powersonic 410, Hwashin, Seoul, Republic of Korea) to get a uniform suspension. In order to obtain uniformly dispersed MR fluid, sufficient shaking and ultrasonic treatment were performed using a vortex mixer (VORTEX Genius 3, IKA, Germany) and ultrasonic processor (Powersonic 410, Hwashin, Seoul, Republic of Korea).

3. Results and Discussion

3.1. Characterization of Synthesized Materials

Figure 1a,d depict the GO sheet's SEM (S-430, Hitachi, Tokyo, Japan) and TEM (CMM-220, Phillips, Boston, MA, USA) images, respectively.

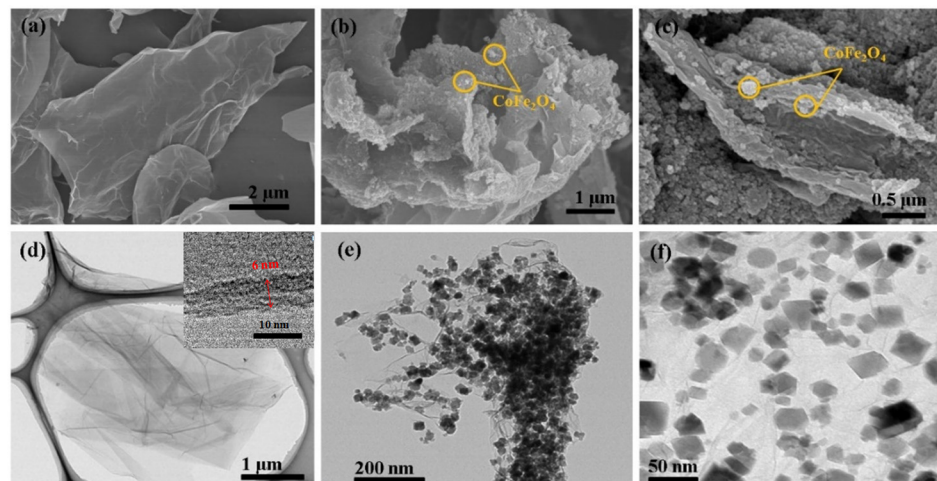


Figure 1. SEM images of (a) GO sheet, (b,c) rGO/CoFe₂O₄, and TEM images of (d) GO sheet, (e,f) rGO/CoFe₂O₄ composite. Inset in (d) shows side view of GO sheet.

The GO sheet's surface appears smooth, and the inset in Figure 1d depicts that the GO sheet's thickness is approximately 6 nm. It is noteworthy that the graphite appears wrinkled after oxidation. This wrinkling phenomenon is due to the oxidation process promoting the introduction of oxygen-containing functional groups, thereby transforming the sp² (planar structure) to sp³ (tetrahedral structure) hybridization [38]. Figure 1b,c,e,f depict the rGO/CoFe₂O₄ composite's SEM and TEM images, respectively. The oxygen-based functional groups on the surface of GO result in a high density of negative charges on its surface. Cobalt and iron cations are electrostatically attracted and adsorbed onto the GO surface. Subsequently, CoFe₂O₄ nanoparticles are formed and anchored onto the GO surface via the solvothermal reaction. Meanwhile, during the solvothermal reaction, GO reduction occurs, resulting in the final rGO/CoFe₂O₄ composite material. As observed, the rGO/CoFe₂O₄ composite's surface exhibits a rougher appearance compared to GO, and the CoFe₂O₄ particles are evenly distributed on the rGO without aggregation. The presence of rGO effectively disperses CoFe₂O₄ particles and avoids agglomeration, increasing the composite's specific surface area [10,39]. In addition, the density of the rGO/CoFe₂O₄ composite was tested to be 4.05 g/cm³ with a gas pycnometer (AccuPyc 1330, micromeritics), notably lower than that of the pure phase CoFe₂O₄ particles (5.29 g/cm³) [40], indicating that the rGO/CoFe₂O₄ composite has a considerable advantage in solving the magnetic particle sedimentation problem in MR fluids.

The sharp diffraction peak indicates a high level of crystallization in the graphite. According to Figure 2a, the diffraction peak of GO is located at 2θ = 10.4°, indicating the (001) lattice plane and a 0.850 nm inter-layer distance. The sharp peak position of GO (001) shifts to the left relative to graphite (002), and the inter-layer distance increases. The increase in inter-layer distance is caused by the introduction of oxygen-containing functional groups during the oxidation of graphite. This indicates that graphite is transformed into GO by the oxidation process. GO exhibits a broad peak at 2θ = 26.4° due to the process efficiency that results in a small amount of graphite not being wholly converted [41]. According to Figure 2b, the characteristic peaks of the CoFe₂O₄ are distinctly observable at 2θ = 18.2°, 29.8°, 35.3°, 37.0°, 42.9°, 53.3°, 56.4°, 61.2°, 70.7°, and 74.0°, which correspond to the lattice planes (111), (220), (311), (222), (400), (422), (511), (440), (620), (533). These diffraction peaks match well with the JCPDS data (#221086) [42]. The positions of the three strongest peaks are 29.8° (220), 35.3° (311), and 61.2° (440), and the space group is Fd-3m (No. 227) [43], which proves that CoFe₂O₄ belongs to the spinel structure. Notably, no (001) GO diffraction peak exists in the rGO/CoFe₂O₄ XRD patterns, which indicates an efficient reduction of GO to rGO [44]. The XRD analysis confirms the successful fabrication of the rGO/CoFe₂O₄ composite.

In Figure 2, the inset reveals that the graphite's XRD (DMAX-2500, Rigaku, Tokyo, Japan) diffraction peak is at $2\theta = 26.4^\circ$, indicating the (002) lattice plane and a 0.336 nm inter-layer distance.

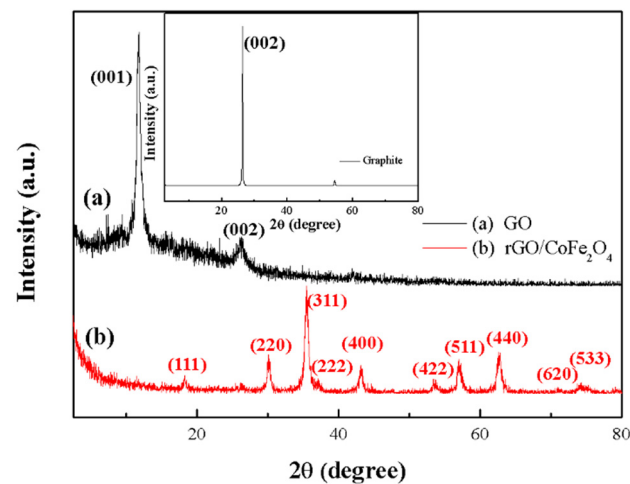


Figure 2. XRD patterns of (a) GO and (b) rGO/CoFe₂O₄. Inset depicts XRD pattern of graphite.

Figure 3 depicts the magnetization curve recorded during the vibrating sample magnetometry (VSM, Lake Shore Cryotronics, Westerville, OH, USA) test of the rGO/CoFe₂O₄ composite at 300 K, with H ranging from -800 kA/m to 800 kA/m.

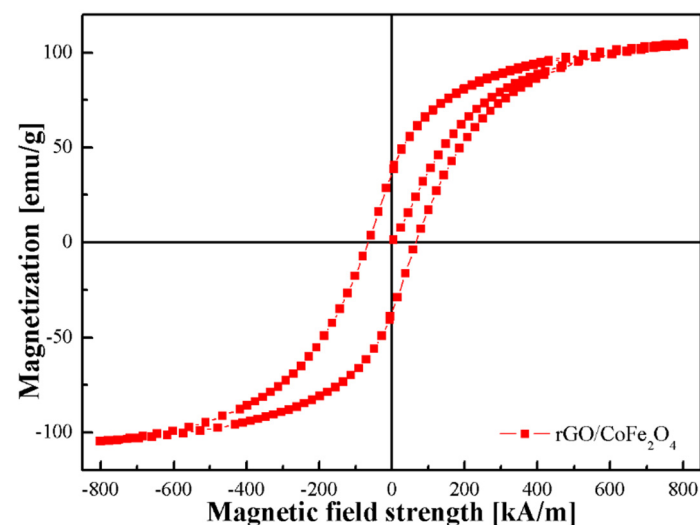


Figure 3. Magnetization curve of rGO/CoFe₂O₄ composite.

The composite has a remanence (M_r) of 34.9 emu/g and a coercivity of 67.7 kA/m (850.7 Oe), which cannot be ignored. Notably, the saturation magnetization (M_s) of the rGO/CoFe₂O₄ composite measures 104.6 emu/g, surpassing the typical value of pure CoFe₂O₄ of 74.08 emu/g [15]. On the one hand, the higher M_s can be explained by the larger particle size of the synthesized CoFe₂O₄ particles [45–48]. On the other hand, compared to pure CoFe₂O₄, the composite of rGO/CoFe₂O₄ affects the super exchange interaction, consequently influencing M_s [49]. This high M_s value is highly desirable because it contributes to enhanced yield strength and rapid response for MR fluids.

3.2. Magnetorheological Effect

3.2.1. Shear Stress and Shear Viscosity

The rGO/CoFe₂O₄-based MR fluid's MR properties were tested with a rotational rheometer (MCR 300, Anton-Paar, Stuttgart, Germany). The shear rate ($\dot{\gamma}$) was set across

a range of 0.01 to 200 1/s, and H in the tests were set to 0, 68, 103, 137, 205, 274, and 342 kA/m. Figure 4a is the log–log graph indicating the relationship between shear stress (τ) and $\dot{\gamma}$ of the rGO/CoFe₂O₄-based MR fluid at different H .

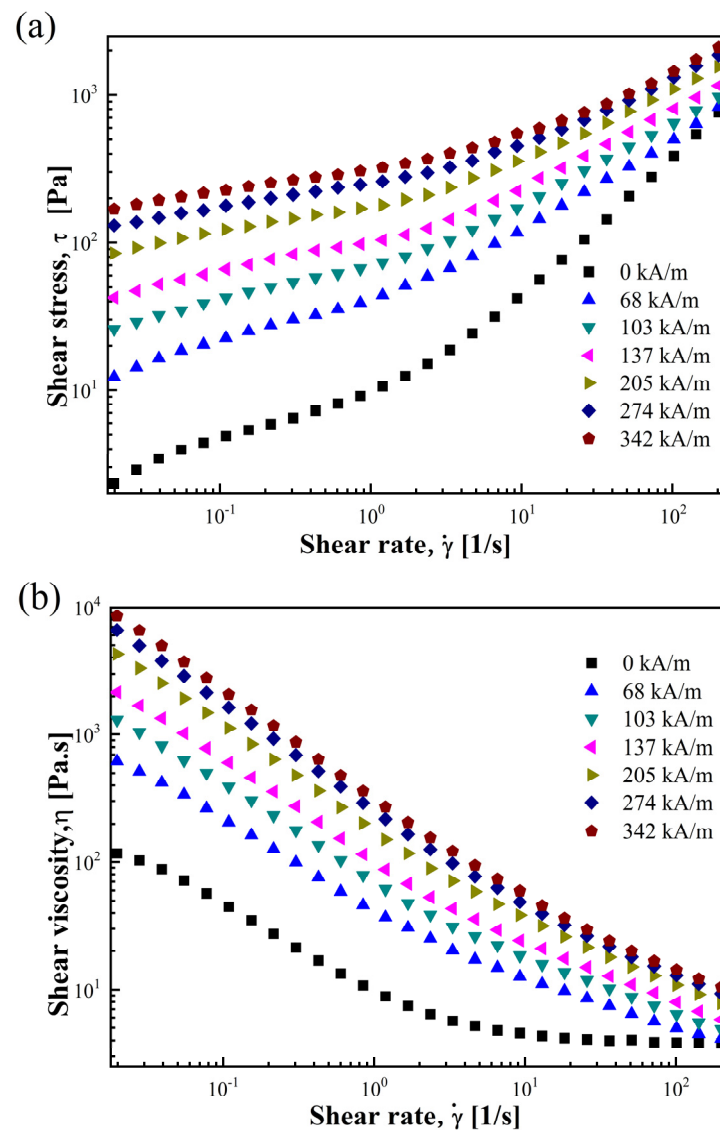


Figure 4. Flow curve for rGO/CoFe₂O₄-based MR fluid under various H (a) shear stress and (b) shear viscosity curves as a function of shear rate.

When H is applied, the τ of the MR fluid is higher than when $H = 0$. At the same $\dot{\gamma}$, the higher the H , the higher the τ . At low $\dot{\gamma}$, the MR fluid at all six H ($H \neq 0$) exhibited high τ , which increased slowly with increasing $\dot{\gamma}$. This is attributed to the strong chain-like structures formed by magnetic dipole–dipole interactions between the rGO/CoFe₂O₄ particles, which are resistant to disruption caused by the increasing $\dot{\gamma}$ [50]. When $\dot{\gamma}$ is high, the MR fluid’s chain-like structure is gradually disrupted, leading to a faster increase in τ with increasing $\dot{\gamma}$.

Figure 4b shows the shear viscosity (η) for rGO/CoFe₂O₄-based MR fluid as a function of $\dot{\gamma}$. It can be observed that η decreases with increasing $\dot{\gamma}$ at different H , suggesting evident shear-thinning behavior. In addition, η significantly increases after the input of H because of the alignment of the rGO/CoFe₂O₄ particles within the MR fluid along the direction of H , forming a chain-like structure. When H increases, the chain-like structure becomes more stable, enhancing resistance to breaking under shear and contributing to a higher η of the MR fluid. However, as $\dot{\gamma}$ increases, the MR fluid’s internal structure gradually

breaks down, causing a decrease in η and showing the shear-thinning characteristic. When $\dot{\gamma}$ is high enough, the change in η is insignificant due to the complete collapse of the chain-like structure.

3.2.2. Storage/Loss Modulus and Relaxation Modulus

To further investigate the rGO/CoFe₂O₄-based MR fluid's viscoelastic behavior, different H (0–342 kA/m) were selected for oscillation tests at a steady 6.28 rad/s frequency. To examine how storage modulus (G') and loss modulus (G'') change in response to strain (γ), γ was set to increase in the range of 0.001–100%. Figure 5a depicts the variation of G' and G'' versus γ for the rGO/CoFe₂O₄-based MR fluid.

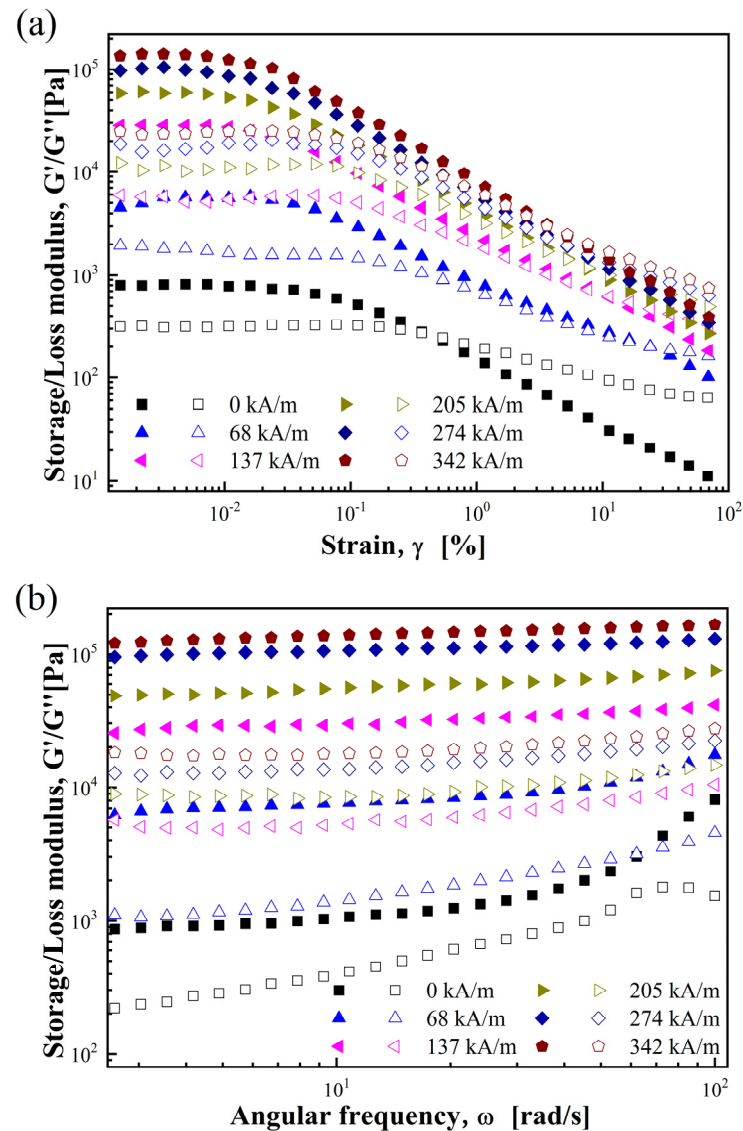


Figure 5. (a) Strain and (b) frequency dependence of storage (closed) and loss (open) modulus for rGO/CoFe₂O₄-based MR fluid.

With an increase in γ , both G' and G'' exhibit a plateau region over a smaller range of γ , recognized as the linear viscoelastic (LVE) region [51], where the G' and G'' remain unaffected by γ . In the LVE region, G' of the rGO/CoFe₂O₄-based MR fluid surpasses G'' , indicating the dominance of its elastic properties and a quasi-solid state. Once γ of the rGO/CoFe₂O₄-based MR fluid exceeds the critical strain of 0.01% here, G' and G'' decrease quickly. When γ surpasses the critical strain, due to the high γ , the chain-like structure within the MR fluid gets disrupted, making the MR fluid change from quasi-solid to fluid.

In response to this transition, there is an irreversible decrease in both G' and G'' , and G' even surpasses G'' when $\dot{\gamma}$ is high.

In the LVE region, a constant γ of 0.01% was applied for frequency sweep tests within the angular frequency (ω) range of 1–100 rad/s. Figure 5b shows the changes of G' and G'' with ω for the rGO/CoFe₂O₄-based MR fluid. Upon applying H , G' and G'' exhibit a plateau region, showing that the MR fluid's internal structure makes it exhibit clear solid-like characteristics rather than liquid ones. The increase in G' due to the increase in H indicates that the stronger H leads to enhanced interparticle interactions, and the MR fluid exhibits a stronger solid-like behavior. Moreover, at a specific H , G' is consistently higher than G'' over a wide ω range, indicating that the rGO/CoFe₂O₄-based MR fluid is mainly characterized by its elastic properties rather than its viscous properties [52].

The time-dependent shear relaxation modulus ($G(t)$) of the rGO/CoFe₂O₄-based MR fluid can be calculated using the Schwarzl equation [53] as follows:

$$G(t) \cong G'(\omega) - 0.560G''(\omega/2) + 0.200G''(\omega) \quad (1)$$

This equation can overcome the limits of mechanical tests and predict the MR fluid's ultrafast relaxation behavior. Figure 6 depicts $G(t)$ in relation to time for the rGO/CoFe₂O₄-based MR fluid.

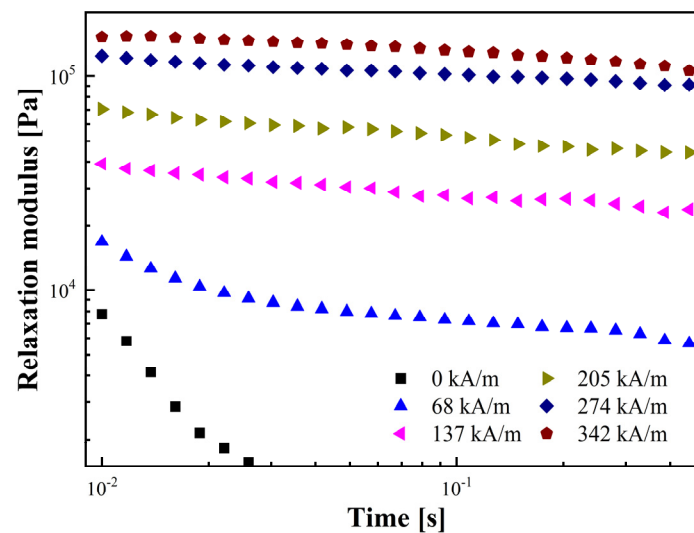


Figure 6. Relaxation modulus calculated from the storage and loss modulus as a function of time.

The evident decrease in $G(t)$ when $H = 0$ indicates the MR fluid's liquid-like behavior. However, the $G(t)$ of the MR fluid demonstrates a plateau state upon application of H , indicating quasi-solid behavior and no stress relaxation in the MR fluid.

3.2.3. Dynamic and Elastic Yield Stress

To effectively consider the impact of $\dot{\gamma}$ on τ , the Herschel–Bulkley model was employed for fitting. When $\dot{\gamma}$ approaches zero, τ can be approximated as the dynamic yield stress (τ_{dy}), as represented in the following equation [54]:

$$\tau = \tau_{dy} + K\dot{\gamma}^n \quad (2)$$

where K is the consistency index; n is the flow behavior index; and $\dot{\gamma}$ is the shear rate.

Table 1 presents the Herschel–Bulkley model's fitting parameters for τ_{dy} , K , and n under various H .

Table 1. Fitting parameters of Herschel–Bulkley model.

$H/(\text{kA/m})$	τ_{dy}	K	n
68	12	27	0.78
103	25	41	0.63
137	42	53	0.59
205	84	76	0.58
274	150	89	0.56
342	200	97	0.56

Notably, all fitted parameters for n are less than 1, indicating shear-thinning behavior in the MR fluid, which aligns with the conclusion drawn from Figure 4b. The solid lines shown in Figure 7a were fitted based on the data from Table 1.

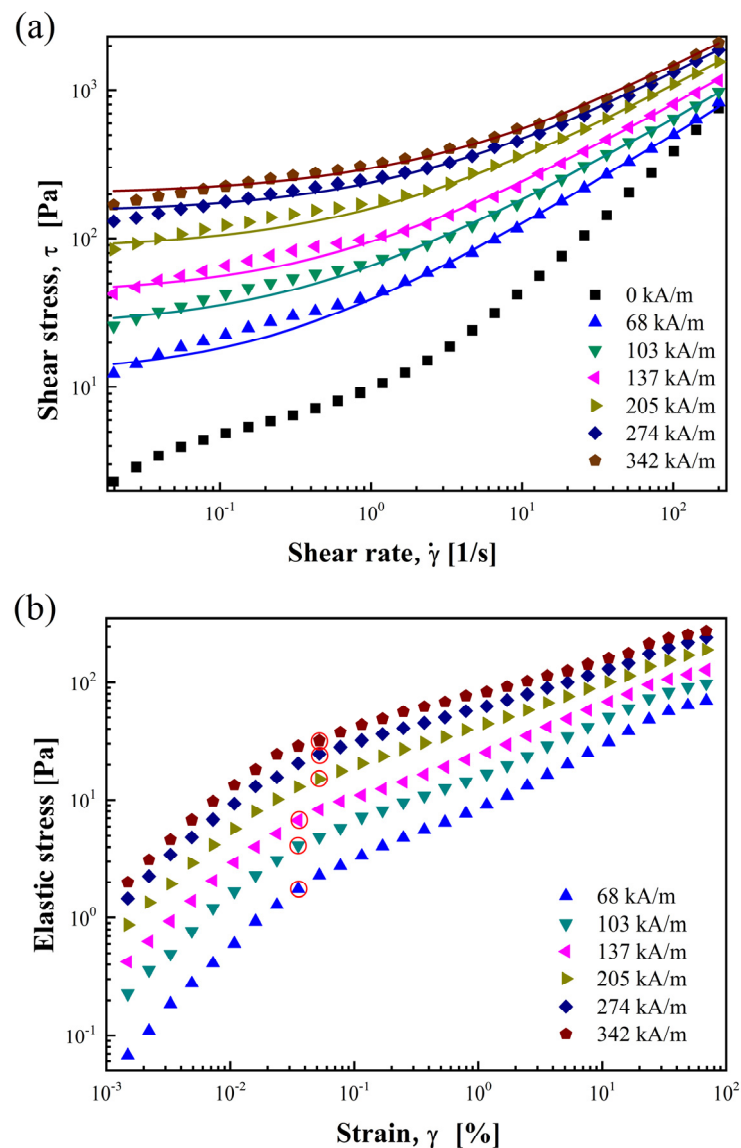


Figure 7. (a) Shear stress as a function of shear rate and (b) elastic stress as a function of strain under various H .

The comparison between the fitting lines and experimental data in Figure 7a demonstrates a high level of agreement, suggesting that the Herschel–Bulkley model effectively fits the rGO/CoFe₂O₄-based MR fluid.

Elastic stress (τ_e) can be determined by applying the following formula to the dynamic oscillatory strain amplitude sweep data:

$$\tau_e = G' \cdot \gamma \quad (3)$$

Figure 7b depicts the functional relationship between τ_e and γ for the rGO/CoFe₂O₄-based MR fluid at various H . Each turning point on the slope of the curve, as indicated by a red circle in the figure, is called the elastic yield point, corresponding to the elastic yield stress (τ_{ey}) at a certain H . On the left side of the elastic yield point, the τ_e of the rGO/CoFe₂O₄-based MR fluid exhibits a linear increase with the rise of γ . However, the rate of increase in τ_e notably decelerates on the right side of the elastic yield point.

Figure 8 shows how τ_{dy} and τ_{ey} change with H . Typically, yield stress (τ_y) and H have a power law relationship as follows:

$$\tau_y \propto H^m \quad (4)$$

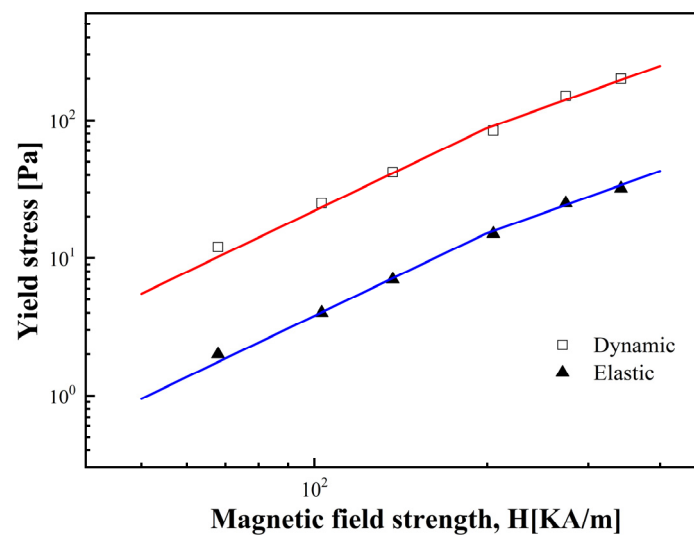


Figure 8. Dynamic yield stress (cubic) and elastic yield stress (trigonal) as function of H .

In the MR fluid, τ_y rises as H increases. When H is low, due to the magnetic polarization of particles, τ_y is directly proportional to H^2 , following [55], as follows:

$$\tau_y \propto \phi \mu_0 H^2 \quad (5)$$

where ϕ represents the MR fluid's volume fraction, and μ_0 is the vacuum magnetic permeability. When H increases, the chain-like structure is less affected by H , and local magnetization saturation dominates τ_y , which can be represented as follows:

$$\tau_y = \sqrt{6} \phi \mu_0 M_s^{1/2} H^{3/2} \quad (6)$$

where M_s represents the saturation magnetization.

From Figure 8, it is evident that as H increases, there exists a critical magnetic field strength (H_c) where the fitted curve's slope shifts from 2.0 to 1.5. Due to the presence of H_c , the relationship between τ_y and H can be expressed using the following general equation [56]:

$$\tau_y(H_0) = \alpha H_0^2 \left(\frac{\tanh \sqrt{H_0/H_C}}{\sqrt{H_0/H_C}} \right) \quad (7)$$

where α depends on the MR fluid’s susceptibility, ϕ , and other physical constants. There are two distinct limiting relations between τ_y and H_0 , as follows:

$$\tau_y = \alpha H_0^2 \quad H_0 \ll H_c \tag{8}$$

$$\tau_y = \alpha \sqrt{H_c} H_0^{3/2} \quad H_0 \gg H_c \tag{9}$$

Equations (8) and (9) indicate that in the case of a low value of H , magnetic particles within the MR fluid are mutually attracted, leading to the creation of chain-like structures.

When H exceeds H_c , the MR fluid gradually becomes saturated, and τ_y is less affected by H . As depicted in Figure 8, the fitted curve’s slope for τ_y as a function of H undergoes a transition as H reaches H_c , demonstrating a high level of agreement with the experimental data.

According to Equation (7), when $H_0 = H_c$, we can obtain $\tau_y(H_0) = \alpha H_0^2 \tanh 1$, which simplifies to $\tau_y(H_0) = 0.762\alpha H_0^2$. From this, we can obtain the following relationship:

$$\hat{\tau} = 1.313 \hat{H}^{3/2} \tanh \sqrt{\hat{H}} \tag{10}$$

where $\hat{\tau} = \tau_{H_0} / \tau_{H_c}$, $\hat{H} = H_0 / H_c$. As depicted in Figure 9, Equation (10) allows the data to be integrated into a unified curve.

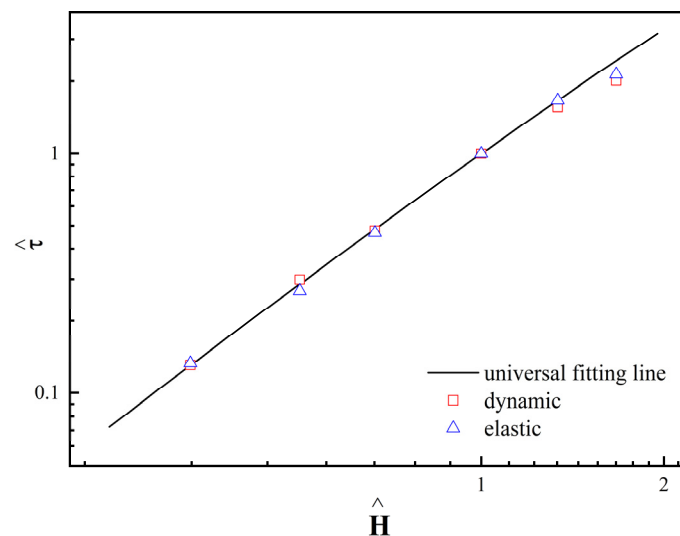


Figure 9. Dynamic and elastic yield stress as a function of H and universal fitting line.

3.2.4. MR Efficiency

MR efficiency quantifies the viscosity gain that can be achieved by the MR fluid at a specific H and $\dot{\gamma}$, which is critical for MR fluids operating in a flow state. The MR efficiency can be obtained by converting the data of the viscosity curve with the following formula:

$$\text{MR efficiency} = \frac{\eta_H - \eta_0}{\eta_0} \times 100\% \tag{11}$$

where η_H and η_0 represent η of the MR fluid at H and 0, respectively. Figure 10 depicts the MR efficiency as a function of $\dot{\gamma}$ and H .

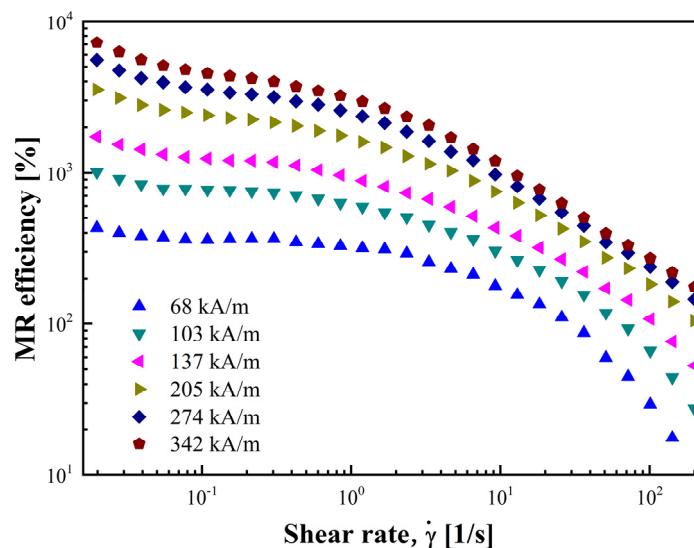


Figure 10. MR efficiency as a function of shear rate under various H .

The graph illustrates a decrease in MR efficiency with an increase in $\dot{\gamma}$. This decrease is due to the gradual disruption of chain-like structures as $\dot{\gamma}$ increases, reducing their resistance to the flow regime. In addition, at a constant $\dot{\gamma}$, increasing H enhances MR efficiency by forming a stronger internal structure that is more rigid to external shear [57]. MR efficiency is essential in engineering, and for MR devices such as dampers that need to operate in a flow state, the yield stress metric is no longer appropriate [58].

4. Conclusions

This work synthesized the rGO/CoFe₂O₄ composite using a solvothermal method. The synthesized GO and rGO/CoFe₂O₄ were characterized using SEM, TEM, and XRD, confirming the successful combination of rGO with CoFe₂O₄ particles. The VSM testing shows an expected high M_s for the rGO/CoFe₂O₄ composite. The flow curves demonstrated the rGO/CoFe₂O₄-based MR fluid's typical MR behaviors. G' and G'' for the MR fluid obtained from oscillation tests reveal its viscoelastic behavior. $G(t)$ was calculated with a Schwarzl equation. For the rGO/CoFe₂O₄-based MR fluid, τ and τ_{dy} conformed well to the Herschel–Bulkley model. Furthermore, τ_y was found to be proportional to H^2 when $H \ll H_c$, while it was proportional to $H^{3/2}$ when $H \gg H_c$. Finally, the rGO/CoFe₂O₄-based MR fluid's MR efficiency was calculated, providing guidance for its potential applications in the flow state. To summarize, the rGO/CoFe₂O₄-based MR fluid can achieve a reversible transition between liquid-like and solid-like states. By applying different magnetic fields, we can control its rheological properties (τ , η , G' and G''). These parameters are the basis for controlling system variables in engineering applications, such as valves, dampers, vehicle suspensions, and engine mounts.

Author Contributions: Conceptualization & methodology, H.J.C., Y.D. and Y.L.; formal analysis, Y.L., Y.D. and H.J.C.; investigation, C.G.; writing—original draft, Y.L.; writing—review & editing, Y.D., H.J.C., C.G. and Y.L. All authors have read and agreed to the published version of the manuscript.

Funding: This research was funded by National Natural Science Foundation of China, grant number 52203329.

Institutional Review Board Statement: Not applicable.

Informed Consent Statement: Not applicable.

Data Availability Statement: Data are contained within the article.

Conflicts of Interest: The authors declare no conflict of interest.

References

1. Ginder, J.M.; Davis, L.C. Shear stresses in magnetorheological fluids: Role of magnetic saturation. *Appl. Phys. Lett.* **1994**, *65*, 3410–3412. [[CrossRef](#)]
2. Zhu, X.; Jing, X.; Cheng, L. Magnetorheological fluid dampers: A review on structure design and analysis. *J. Intell. Mater. Syst. Struct.* **2012**, *23*, 839–873. [[CrossRef](#)]
3. Goncalves, F.D.; Ahmadian, M.; Carlson, J.D. Investigating the magnetorheological effect at high flow velocities. *Smart Mater. Struct.* **2006**, *15*, 75–85. [[CrossRef](#)]
4. de Vicente, J.; Klingenberg, D.J.; Hidalgo-Alvarez, R. Magnetorheological fluids: A review. *Soft Matter* **2011**, *7*, 3701–3710. [[CrossRef](#)]
5. Olabi, A.G.; Grunwald, A. Design and application of magneto-rheological fluid. *Mater. Des.* **2007**, *28*, 2658–2664. [[CrossRef](#)]
6. Wang, M.; Nie, M.; Liu, Y.; Guo, H. Simulation of Magnetorheological Plane Polishing Scratch Creation Process and Suppression Method. *Machines* **2022**, *10*, 812. [[CrossRef](#)]
7. Masa'id, A.; Lenggana, B.W.; Ubaidillah, U.; Susilo, D.D.; Choi, S.-B. A Review on Vibration Control Strategies Using Magnetorheological Materials Actuators: Application Perspective. *Actuators* **2023**, *12*, 113. [[CrossRef](#)]
8. Li, G.; Ruan, Z.; Gu, R.; Hu, G. Fuzzy Sliding Mode Control of Vehicle Magnetorheological Semi-Active Air Suspension. *Appl. Sci.* **2021**, *11*, 10925. [[CrossRef](#)]
9. Yang, J.; Sun, S.; Yang, X.; Ma, Y.; Yun, G.; Chang, R.; Tang, S.-Y.; Nakano, M.; Li, Z.; Du, H.; et al. Equipping New SMA Artificial Muscles With Controllable MRF Exoskeletons for Robotic Manipulators and Grippers. *IEEE/ASME Trans. Mechatron.* **2022**, *27*, 4585–4596. [[CrossRef](#)]
10. Jiang, Y.; Chen, D.; Yang, W.; Wu, S.; Luo, X. Reduced graphene oxide enhanced magnetic nanocomposites for removal of carbamazepine. *J. Mater. Sci.* **2018**, *53*, 15474–15486. [[CrossRef](#)]
11. Eshgarf, H.; Ahmadi Nadooshan, A.; Raisi, A. An overview on properties and applications of magnetorheological fluids: Dampers, batteries, valves and brakes. *J. Energy Storage* **2022**, *50*, 104648. [[CrossRef](#)]
12. Ashtiani, M.; Hashemabadi, S.H.; Ghaffari, A. A review on the magnetorheological fluid preparation and stabilization. *J. Magn. Magn. Mater.* **2015**, *374*, 716–730. [[CrossRef](#)]
13. Lee, J.Y.; Kwon, S.H.; Choi, H.J. Magnetorheological characteristics of carbonyl iron microparticles with different shapes. *Korea-Aust. Rheol. J.* **2019**, *31*, 41–47. [[CrossRef](#)]
14. Zhu, W.; Dong, X.; Huang, H.; Qi, M. Iron nanoparticles-based magnetorheological fluids: A balance between MR effect and sedimentation stability. *J. Magn. Magn. Mater.* **2019**, *491*, 165556. [[CrossRef](#)]
15. Zi, Z.; Sun, Y.; Zhu, X.; Yang, Z.; Dai, J.; Song, W. Synthesis and magnetic properties of CoFe₂O₄ ferrite nanoparticles. *J. Magn. Magn. Mater.* **2009**, *321*, 1251–1255. [[CrossRef](#)]
16. Zhang, K.; Piao, S.H.; Choi, H.J. Hollow Structured Magnetic Particles of CoFe₂O₄ and Their Magnetorheological Characteristics. *IEEE Trans. Magn.* **2015**, *51*, 2005904. [[CrossRef](#)]
17. Wang, G.; Zhou, F.; Lu, Z.; Ma, Y.; Li, X.; Tong, Y.; Dong, X. Controlled synthesis of CoFe₂O₄/MoS₂ nanocomposites with excellent sedimentation stability for magnetorheological fluid. *J. Ind. Eng. Chem.* **2019**, *70*, 439–446. [[CrossRef](#)]
18. Gusynin, V.P.; Sharapov, S.G. Unconventional integer quantum Hall effect in graphene. *Phys. Rev. Lett.* **2005**, *95*, 146801. [[CrossRef](#)]
19. Wang, Y.; Huang, Y.; Song, Y.; Zhang, X.; Ma, Y.; Liang, J.; Chen, Y. Room-temperature ferromagnetism of graphene. *Nano Lett.* **2009**, *9*, 220–224. [[CrossRef](#)]
20. Soldano, C.; Mahmood, A.; Dujardin, E. Production, properties and potential of graphene. *Carbon* **2010**, *48*, 2127–2150. [[CrossRef](#)]
21. Lee, C.; Wei, X.; Kysar, J.W.; Hone, J. Measurement of the elastic properties and intrinsic strength of monolayer graphene. *Science* **2008**, *321*, 385–388. [[CrossRef](#)]
22. Bunch, J.S.; Verbridge, S.S.; Alden, J.S.; van der Zande, A.M.; Parpia, J.M.; Craighead, H.G.; McEuen, P.L. Impermeable atomic membranes from graphene sheets. *Nano Lett.* **2008**, *8*, 2458–2462. [[CrossRef](#)] [[PubMed](#)]
23. Balandin, A.A.; Ghosh, S.; Bao, W.; Calizo, I.; Teweldebrhan, D.; Miao, F.; Lau, C.N. Superior thermal conductivity of single-layer graphene. *Nano Lett.* **2008**, *8*, 902–907. [[CrossRef](#)] [[PubMed](#)]
24. Wang, X.; Zhi, L.; Mullen, K. Transparent, conductive graphene electrodes for dye-sensitized solar cells. *Nano Lett.* **2008**, *8*, 323–327. [[CrossRef](#)] [[PubMed](#)]
25. Knapek, A.; Sobola, D.; Burda, D.; Danhel, A.; Mousa, M.; Kolarik, V. Polymer Graphite Pencil Lead as a Cheap Alternative for Classic Conductive SPM Probes. *Nanomaterials* **2019**, *9*, 1756. [[CrossRef](#)]
26. Tiwari, S.K.; Mishra, R.K.; Ha, S.K.; Huczko, A. Evolution of Graphene Oxide and Graphene: From Imagination to Industrialization. *ChemNanoMat* **2018**, *4*, 598–620. [[CrossRef](#)]
27. Dikin, D.A.; Stankovich, S.; Zimney, E.J.; Piner, R.D.; Dommett, G.H.; Evmenenko, G.; Nguyen, S.T.; Ruoff, R.S. Preparation and characterization of graphene oxide paper. *Nature* **2007**, *448*, 457–460. [[CrossRef](#)] [[PubMed](#)]
28. Geim, A.K. Graphene: Status and prospects. *Science* **2009**, *324*, 1530–1534. [[CrossRef](#)]
29. Zhu, Y.; Murali, S.; Cai, W.; Li, X.; Suk, J.W.; Potts, J.R.; Ruoff, R.S. Graphene and graphene oxide: Synthesis, properties, and applications. *Adv. Mater.* **2010**, *22*, 3906–3924. [[CrossRef](#)]
30. Park, S.; Ruoff, R.S. Chemical methods for the production of graphenes. *Nat. Nanotechnol.* **2009**, *4*, 217–224. [[CrossRef](#)]

31. Buchsteiner, A.; Lerf, A.; Pieper, J. Water dynamics in graphite oxide investigated with neutron scattering. *J. Phys. Chem. B* **2006**, *110*, 22328–22338. [[CrossRef](#)] [[PubMed](#)]
32. Seredych, M.; Tamashauskyy, A.V.; Bandoz, T.J. Graphite oxides obtained from porous graphite: The role of surface chemistry and texture in ammonia retention at ambient conditions. *Adv. Funct. Mater.* **2010**, *20*, 1670–1679. [[CrossRef](#)]
33. Huang, Y.; Ding, X.; Li, S.; Zhang, N.; Wang, J. Magnetic reduced graphene oxide nanocomposite as an effective electromagnetic wave absorber and its absorbing mechanism. *Ceram. Int.* **2016**, *42*, 17116–17122. [[CrossRef](#)]
34. Xie, Y.L.; An, J.X.; Shi, P.Z.; Ye, N.S. Determination of Lysozyme by Graphene Oxide-Polyethylene Glycol-Based Fluorescence Resonance Energy Transfer. *Anal. Lett.* **2017**, *50*, 148–160. [[CrossRef](#)]
35. Yavuz, E.; Tokalioglu, S.; Sahan, H.; Kaçer, M.; Patat, S. Dispersive Solid-Phase Extraction of Rhodium from Water, Street Dust, and Catalytic Converters Using a Cellulose-Graphite Oxide Composite. *Anal. Lett.* **2017**, *50*, 63–79. [[CrossRef](#)]
36. Hummers, W.S.; Offeman, R.E. Preparation of Graphitic Oxide. *J. Am. Chem. Soc.* **1958**, *80*, 1339. [[CrossRef](#)]
37. Choi, H.-Y.; Choi, J.-Y.; Park, H.-H.; Kim, T.-H.; Choi, H.J.; Lee, C.-S. Effect of reduced graphene oxide and MnFe₂O₄ nanoparticles on carbonyl iron for magnetorheological fluids. *J. Ind. Eng. Chem.* **2021**, *98*, 140–147. [[CrossRef](#)]
38. Hack, R.; Correia, C.H.G.; Zanon, R.A.d.S.; Pezzin, S.H. Characterization of graphene nanosheets obtained by a modified Hummer's method. *Matéria* **2018**, *23*, e-11988. [[CrossRef](#)]
39. Chen, T.; Du, P.; Jiang, W.; Liu, J.; Hao, G.; Gao, H.; Xiao, L.; Ke, X.; Zhao, F.; Xuan, C. A facile one-pot solvothermal synthesis of CoFe₂O₄/RGO and its excellent catalytic activity on thermal decomposition of ammonium perchlorate. *RSC Adv.* **2016**, *6*, 83838–83847. [[CrossRef](#)]
40. Dedi; Idayanti, N.; Kristiantoro, T.; Alarn, G.F.N.; Sudrajat, N. Magnetic Properties of Cobalt Ferrite Synthesized by Mechanical Alloying. In Proceedings of the 1st International Seminar on Metallurgy and Materials (ISMM), Jakarta, Indonesia, 24–25 October 2017. [[CrossRef](#)]
41. Rao, S.; Upadhyay, J.; Polychronopoulou, K.; Umer, R.; Das, R. Reduced Graphene Oxide: Effect of Reduction on Electrical Conductivity. *J. Compos. Sci.* **2018**, *2*, 25. [[CrossRef](#)]
42. Mitra, S.; Veluri, P.S.; Chakraborty, A.; Petla, R.K. Electrochemical Properties of Spinel Cobalt Ferrite Nanoparticles with Sodium Alginate as Interactive Binder. *ChemElectroChem* **2014**, *1*, 1068–1074. [[CrossRef](#)]
43. Fritsch, D.; Ederer, C. First-principles calculation of magnetoelastic coefficients and magnetostriction in the spinel ferrites CoFe₂O₄ and NiFe₂O₄. *Phys. Rev. B* **2012**, *86*, 014406. [[CrossRef](#)]
44. Yao, Y.; Yang, Z.; Zhang, D.; Peng, W.; Sun, H.; Wang, S. Magnetic CoFe₂O₄-Graphene Hybrids: Facile Synthesis, Characterization, and Catalytic Properties. *Ind. Eng. Chem. Res.* **2012**, *51*, 6044–6051. [[CrossRef](#)]
45. Liu, C.; Rondinone, A.J.; Zhang, Z.J. Synthesis of magnetic spinel ferrite CoFe₂O₄ nanoparticles from ferric salt and characterization of the size-dependent superparamagnetic properties. *Pure Appl. Chem.* **2000**, *72*, 37–45. [[CrossRef](#)]
46. Hu, L.; Li, M.; Cheng, L.; Jiang, B.; Ai, J. Solvothermal synthesis of octahedral and magnetic CoFe₂O₄-reduced graphene oxide hybrids and their photo-Fenton-like behavior under visible-light irradiation. *RSC Adv.* **2021**, *11*, 22250–22263. [[CrossRef](#)] [[PubMed](#)]
47. Goh, S.C.; Chia, C.H.; Zakaria, S.; Yusoff, M.; Haw, C.Y.; Ahmadi, S.; Huang, N.M.; Lim, H.N. Hydrothermal preparation of high saturation magnetization and coercivity cobalt ferrite nanocrystals without subsequent calcination. *Mater. Chem. Phys.* **2010**, *120*, 31–35. [[CrossRef](#)]
48. Mazarji, M.; Esmaili, H.; Bidhendi, G.N.; Mahmoodi, N.M.; Minkina, T.; Sushkova, S.; Mandzhieva, S.; Barakhov, A.; Moghtaderi, H.; Bhatnagar, A. Green synthesis of reduced graphene oxide-CoFe₂O₄ nanocomposite as a highly efficient visible-light-driven catalyst in photocatalysis and photo Fenton-like reaction. *Mater. Sci. Eng. B* **2021**, *270*, 115223. [[CrossRef](#)]
49. Devi, L.G.; Srinivas, M. Hydrothermal synthesis of reduced graphene oxide-CoFe₂O₄ heteroarchitecture for high visible light photocatalytic activity: Exploration of efficiency, stability and mechanistic pathways. *J. Environ. Chem. Eng.* **2017**, *5*, 3243–3255. [[CrossRef](#)]
50. Zhang, J.Q.; Zhang, J.; Kong, Y.N.; Cuan, H.L. Dynamical Simulation of Magnetorheological Fluid Characteristics. *Adv. Mater. Res.* **2011**, *255–260*, 3505–3509. [[CrossRef](#)]
51. Agirre-Olabide, I.; Berasategui, J.; Elejabarrieta, M.J.; Bou-Ali, M.M. Characterization of the linear viscoelastic region of magnetorheological elastomers. *J. Intell. Mater. Syst. Struct.* **2014**, *25*, 2074–2081. [[CrossRef](#)]
52. Kim, Y.J.; Liu, Y.D.; Seo, Y.; Choi, H.J. Pickering-emulsion-polymerized polystyrene/Fe₂O₃ composite particles and their magnetoresponsive characteristics. *Langmuir* **2013**, *29*, 4959–4965. [[CrossRef](#)] [[PubMed](#)]
53. Schwarzl, F.R. Numerical calculation of storage and loss modulus from stress relaxation data for linear viscoelastic materials. *Rheol. Acta* **1971**, *10*, 165–173. [[CrossRef](#)]
54. Versaci, M.; Palumbo, A. Magnetorheological Fluids: Qualitative comparison between a mixture model in the Extended Irreversible Thermodynamics framework and an Herschel-Bulkley experimental elastoviscoplastic model. *Int. J. Non-Linear Mech.* **2020**, *118*, 103228. [[CrossRef](#)]
55. Maurya, C.S.; Sarkar, C. Effect of Fe₃O₄ Nanoparticles on Magnetorheological Properties of Flake-Shaped Carbonyl Iron Water-Based Suspension. *IEEE Trans. Magn.* **2020**, *56*, 4600608. [[CrossRef](#)]
56. Choi, H.J.; Cho, M.S.; Kim, J.W.; Kim, C.A.; Jhon, M.S. A yield stress scaling function for electrorheological fluids. *Appl. Phys. Lett.* **2001**, *78*, 3806–3808. [[CrossRef](#)]

57. Arief, I.; Mukhopadhyay, P.K. Dynamic and rate-dependent yielding behavior of $\text{Co}_{0.9}\text{Ni}_{0.1}$ microcluster based magnetorheological fluids. *J. Magn. Magn. Mater.* **2016**, *397*, 57–63. [[CrossRef](#)]
58. Lopez-Lopez, M.T.; Gomez-Ramirez, A.; Rodriguez-Arco, L.; Duran, J.D.; Iskakova, L.; Zubarev, A. Colloids on the frontier of ferrofluids. Rheological properties. *Langmuir* **2012**, *28*, 6232–6245. [[CrossRef](#)]

Disclaimer/Publisher's Note: The statements, opinions and data contained in all publications are solely those of the individual author(s) and contributor(s) and not of MDPI and/or the editor(s). MDPI and/or the editor(s) disclaim responsibility for any injury to people or property resulting from any ideas, methods, instructions or products referred to in the content.